Individualized cyclic mechanical loading improves callus properties during the remodelling phase of fracture healing in mice as assessed from time-lapsed *in vivo* imaging

Esther Wehrle[1*], Graeme R Paul[1], Duncan C Tourolle né Betts[1], Gisela A Kuhn[1], Ralph Müller[1*]

[1] Institute for Biomechanics, ETH Zurich, Zurich, Switzerland.

Corresponding authors:

Esther Wehrle, PhD, DVM

Institute for Biomechanics, ETH Zurich

Leopold-Ruzicka-Weg 4

8093 Zurich, Switzerland

Email: esther.wehrle@hest.ethz.ch

Ralph Müller, PhD

Institute for Biomechanics, ETH Zurich

Leopold-Ruzicka-Weg 4

8093 Zurich, Switzerland

Email: ram@ethz.ch

Abstract

Fracture healing is regulated by mechanical loading. Understanding the underlying mechanisms during the different healing phases is required for targeted mechanical intervention therapies. Here, the influence of individualized cyclic mechanical loading on the remodelling phase of fracture healing was assessed in a mouse femur defect model. After bridging of the defect, a loading group (n=10) received individualized cyclic mechanical loading (8-16 N, 10 Hz, 5 min, 3x/week) based on computed strain distribution in the callus using animal-specific real-time micro-finite element analysis. Controls (n=10) received 0 N treatment at the same post-operative time-points. By registration of consecutive scans, structural and dynamic callus morphometric parameters were followed in three callus sub-volumes and the adjacent cortex showing that the remodelling phase of fracture healing is highly responsive to cyclic mechanical loading with changes in dynamic parameters leading to significantly larger callus formation and mineralization. Loading-mediated maintenance of callus remodelling was associated with distinct effects on Wnt-signalling-associated molecular targets Sclerostin and RANKL in callus sub-regions and the adjacent cortex. Given these distinct local protein expression patterns induced by cyclic mechanical loading, the femur defect loading model with individualized load application seems suitable to understand the local spatio-temporal mechano-molecular regulation of the different fracture healing phases.

Introduction

Mechanical loading is a key factor for normal progression of the fracture healing process. Delayed fracture repair and non-union formation is a major issue in orthopaedic surgery, with an incidence of 5-10% and a high socioeconomic burden [1,2] and has been partially attributed to low and inadequate mechanical loading of the defect region [3,4], affecting all consecutive phases (inflammation, repair, remodelling) of the fracture repair process. The local mechanical conditions in the fracture healing area (for details see tissue differentiation hypothesis by Claes & Heigele [5]) are crucial for the repair process by determining molecular and cellular reactions, the tissue to be formed and the type of ossification. We and others have previously shown that externally applied mechanical stimuli, either applied locally to the fracture site via dynamic fixators [6] or globally via whole body vibration platforms [7,8], can improve fracture healing. In contrast, inadequate mechanical stimuli resulting in a too low or too high interfragmentary motion were not successful or even impaired the healing process [9-11]; for review see [12]). In order to understand the underlying mechanisms, refined and well controlled *in vivo* loading models are needed. Recent studies particularly indicate that profound understanding of the local spatio-temporal mechanical regulation of the fracture healing process seems crucial for translation of this knowledge to the clinics, aiming at the development of safe, targeted and individualized mechanical intervention therapies. Whereas many preclinical fracture healing studies focused on improving the early healing phases (inflammation, repair) with the aim of increasing bone formation and achieving earlier bone union, recent studies also indicate a potential to improve long-bone fracture healing outcome via modulation of callus remodelling [13-15]. Given the strong influence of mechanical loading on normal bone remodelling, the application of controlled mechanical loading might be suitable

to also improve and accelerate the remodelling phase during fracture healing. However, preclinical fracture healing studies with application of loading have so far shown contradictory results [12] and have not been able to completely capture underlying mechanisms due to restrictions in study design: (I) cross-sectional setup with only end-point analyses, (II) effect assessment not specific to healing phases, (III) same load for all animals irrespective of individual callus properties and healing progression. We aim to overcome current limitations by combining state-of-the-art time-lapsed *in vivo* imaging with a novel precisely controlled femur defect loading system in mice. By applying time-lapsed *in vivo* micro-CT and animal-specific real-time micro-finite element (RTFE) analysis, the developed femur defect loading model allows scaling of loading settings based on strain distribution in the callus[16], thereby considering individual differences in healing speed. To follow the healing progression in each animal, a recently developed longitudinal *in vivo* micro-CT based approach was applied, which was previously shown to capture the different healing phases and to discriminate physiological and impaired healing patterns[17], without significant radiation-associated effects on callus properties [18]. By registering consecutive scans of the defect region for each animal and implementing a two-threshold approach, data on bone turnover and mineralization kinetics can be obtained, which is particularly important for targeting callus remodelling under different conditions.

The objective of this study was to assess the influence of individualized cyclic mechanical loading on the remodelling phase of fracture healing via longitudinal *in vivo* micro-CT imaging. We hypothesized, that individualized cyclic mechanical loading improves structural and dynamic callus properties during the remodelling phase of fracture healing.

The study showed that the remodelling phase of fracture healing is highly responsive to cyclic mechanical loading leading to significantly larger callus formation and mineralization. Loading-mediated maintenance of callus remodelling was associated with distinct effects on Wnt-signalling-associated molecular targets Sclerostin and RANKL in callus sub-regions and the adjacent cortex. The tightly controlled femur defect loading model could widen our knowledge on the local spatio-temporal mechano-molecular regulation of fracture healing relevant for application of mechanical intervention therapies to clinical settings for improvement of impaired healing conditions.

Results

By combining a novel *in vivo* femur defect loading model (Fig. 1) with a recently established time-lapsed *in vivo* micro-CT based monitoring approach [18,19], the influence of individualized cyclic mechanical loading on callus properties was assessed during the remodelling phase of fracture healing. A loading group (n=10) received individualized cyclic mechanical loading (8-16 N, 10 Hz, 5 min, 3x/week) based on computed strain distribution in the callus using animal-specific RTFE, whereas controls (n=10) received 0N for 5 min at the same post-operative time-points. By registration of consecutive scans, structural and dynamic callus parameters were followed in three callus sub-volumes (defect centre: DC, defect periphery: DP, cortical fragment periphery: FP, and the adjacent cortical fragments: FC over time (Fig. 2 and 3). For details on methods see Tourolle et al. 2019 [19]; for detailed study design see Supplementary Table S1.

General physical observation

109 All mice recovered rapidly from surgery. During the healing period, the animals' body weight
110 did not significantly change compared to pre-operative values without significant differences
111 between or within the two groups (see Supplementary Fig. S2). We also assessed the social
112 interaction between mice (animals sitting in groups vs. separated from others) and the nesting
113 behaviour (start of nest building after surgery). Specifically, all animals started to build nests
114 on the day of surgery and were found in groups in the nest in the morning of post-operative
115 day 1. Throughout the further healing period social interaction between mice and nesting
116 behaviour did not differ from pre-surgical observations and was similar for animals of the
117 loading and control groups.
118

119 **Volumes of interest (VOI) for evaluation by time-lapsed *in vivo* micro-CT**

120 In order to exclude bias in the further micro-CT analyses, we compared the size of the different
121 VOIs (depicted in Fig. 3; for details on VOI generation see Tourolle et al., 2020 [19]). The VOIs
122 encompassed the following volume for the control (n=10) and the loading group (n=10):
123 1.14±0.13mm^3 vs. 1.04±0.16mm^3 for the defect centre (DC), 6.68±0.77mm^3 vs. 6.35±0.82mm^3
124 for the defect periphery (DP), 2.28±0.17mm^3 vs. 2.31±0.16mm^3 for the cortical fragments (FC),
125 15.44±0.70mm^3 vs. 15.84±0.99mm^3 for the fragment periphery (FP). No significant differences
126 in volume were detected in any of the VOIs between groups.
127

128 **Pre-loading healing patterns monitored by time-lapsed *in vivo* micro-CT**

129 In the pre-loading healing period (week 0 to week 3) similar and physiological healing patterns
130 were observed for the control group (n=10) and the loading group (n=10) in all defect VOIs
131 (DC, DP and FP) and the adjacent cortex (FC; Fig. 2 and 3). Registration of consecutive *in vivo*

132 micro-CT scans allowed to capture distinct callus characteristics indicative of the different
133 healing phases (inflammation, repair, remodelling; significant weekly differences in bone
134 parameters indicated in Fig. 3). From week 0-1 to week 1-2 in both groups a significant 4x to
135 14x increase in bone formation was detected in the three callus VOIs DC (control group:
136 $p=0.0007$; loading group: $p=0.0006$; Fig. 3a), DP (control group: $p<0.0001$; loading group:
137 $p<0.0001$; Fig. 3d) and FP (control group: $p=0.0012$; loading group: $p=0.0006$; Fig. 3j),
138 indicating progression from the inflammation to the reparative phase. This led to a significant
139 gain in bone volume (BV/TV) by week 2 in the callus VOIs DC (control group: $p<0.0001$; loading
140 group: $p<0.0001$; Fig. 3b), DP (control group: $p<0.0001$; loading group: $p<0.0001$; Fig. 3e) and
141 FP (control group: $p<0.0001$; loading group: $p<0.0001$; Fig. 3k). From week 1-2 to week 2-3 a
142 significant 3x to 9x increase in resorptive activities was seen in the callus VOIs DC (control
143 group: $p=0.0023$; loading group: $p<0.0001$; Fig. 3a), DP (control group: $p=0.0499$; loading
144 group: $p=0.0162$; Fig. 3d) and FP (control group: $p=0.0326$; loading group: $p=0.0070$; Fig. 3j),
145 indicating the progression from the repair to the remodelling phase. From week 2 to week 3,
146 the highly mineralized bone fraction in the callus VOIs significantly increased ($p<0.0001$ in DC,
147 DP, FP) in both groups, indicating callus maturation (Fig. 3c, 3f and 3l).
148 From week 0 to week 3, in both groups, strong resorptive activities (Fig. 2 and 3g) were seen
149 in the adjacent cortical fragments (FC). BRR showed significant weekly increases whereas no
150 significant weekly changes in bone formation were observed in this VOI. The strong resorptive
151 activities let to decreased bone volume by week 3 reaching statistical significance in the
152 loading group ($p<0.0001$). Furthermore, the fraction of highly mineralized bone significantly
153 decreased from week 1 to week 3 in both groups ($p<0.0001$), indicating cortical
154 reorganisation.

Individualized cyclic mechanical loading improves callus properties during the remodelling phase of fracture healing

Individualized cyclic mechanical loading (8-16N, 10 Hz, 300 cycles, 3x/week) started after bridging of the femur defect (week 3; Table 1) at the beginning of the remodelling phase (loading group, n=10). RTFE allowed determination of initial loads (8-12N) based on individual callus properties, weekly load-scaling (8-16N) and matching of strain distribution in the callus for the 4-week loading period. Control animals received 0N loading at the same post-operative time-points. Already after 1 week, the first loading-associated effects on callus properties and the adjacent cortical bone were seen: Specifically, loading reduced BRR in all VOIs in week 3-4 compared to pre-loading values in week 2-3 (Fig. 3a, d, g, j) reaching statistical significance in DC ($p<0.0001$). In contrast, in the control group, BRR further increased in all VOIS during the same period with statistical significance seen in the peripheral VOIs ($p=0.0066$ for DP, $p=0.0126$ for FP). From week 3-4 to week 6-7, the applied individualized mechanical loading was also able to maintain bone formation at significantly higher levels compared to controls, while bone resorption was significantly reduced during the same period. This led to a linear increase in osseous callus volume in loaded animals from week 3 to week 7 in all callus VOIs (DC: +41 %, DP: +130 %, FP: +111 %) and the adjacent cortex (FC: +20 %), whereas it significantly declined in controls (DC: - 28 %, DP: - 44 %, FP: -27 %, FC: -30 %). In week 6-7, no significant differences in bone turnover were seen anymore indicating load adaptation. After 7 weeks, loaded animals had significantly more bone in the defect (2x for DC, $p<0.0001$; 4x for DP, $p<0.0001$; 3x for FP, $p<0.0001$) with a significantly larger fraction of highly mineralized bone compared to controls (+8% for DC, $p=0.0006$; +15% for DP, $p<0.0015$; +10% for FP,

178 p<0.0001). Three-point bending also showed a 46% higher relative bending stiffness (healed
179 femur vs. contralateral femur) in the loaded animals (107%) compared to controls (73%;
180 n=2/group; Supplementary Fig. S3). In addition, according to the standard clinical evaluation
181 of X-rays, the number of bridged cortices per callus was evaluated in two perpendicular planes
182 and animals with ≥3 bridged cortices were categorized as healed. From week 4 to week 7 all
183 defects in both groups were categorized as healed (Table 1), indicating that the applied forces
184 during cyclic mechanical loading did not lead to re-fracture of the callus.
185 Loading also affected the bone turnover in the adjacent cortex (FC). Already after 1 week,
186 loaded animals showed significantly lower cortical bone resorption compared to controls (Fig.
187 3 j). Whereas cortical volume significantly declined (p<0.0001) in control animals from week 3
188 to week 7 by 27%, it significantly increased (p<0.0001) by 20% in the loaded animals during
189 the same time period (Fig. 3k). From week 4 to week 7 loading was also associated with
190 significantly higher cortical mineralization (+4% in week 4 to +54% in week 7) compared to
191 controls (week 4: p=0.0459, week 5 – week 7: p<0.0001; Fig. 3l).
192 In week 7, the FC VOI comprised 46% and 34% of the osseous tissue in the total VOI (TOT) for
193 the control and loading group, respectively. In the DC VOI, 20% (control group) and 17%
194 (loading group) of the total bone volume were seen. In the two peripheral VOIs, 9% (control
195 group) and 14% (loading group) of the total osseous tissue were seen in the DP and 26%
196 (control group) and 35% (loading group) in the FP VOI. Loading was associated with a shift in
197 the bone distribution from the cortical fragments to the peripheral VOIs.
198
199 **Histology**

200 In order to also visualize the tissue composition of the callus, we performed end point
201 histological stainings of serial sections from one animal of each group. Histology supported
202 our micro-CT findings with complete cortical bridging seen in the animal from the loading and
203 from the control group (Fig. 4 B-I). However, the loaded animal showed a larger callus with
204 some cartilage fractions suggesting ongoing endochondral ossification processes, whereas in
205 the control animal the callus was largely remodelled with restoration of the medullary cavity
206 indicating proceeding towards the end of healing (Fig. 4 b-e). Furthermore, differences in the
207 shape of the cell nuclei were observed between the osteocytes in the fracture callus (round
208 shape) of the loaded animal in comparison to the cell nuclei seen in the cortical bone of the
209 same animal (ellipsoidal shape) and the cell morphology seen in the control animals (Fig. 5
210 a+b), suggesting an association between the local mechanical environment and cellular
211 morphology. In regions with lower strains visualized by micro-FE (endosteal fracture callus;
212 Fig. 4a and 5b), rounder cell nuclei were observed, compared to ellipsoidal nuclei shape in
213 higher strained regions (cortex; Fig. 4a and 5b). To capture potential underlying mechano-
214 molecular targets, we performed immunohistochemistry of Sclerostin (inhibitor of the
215 mechano-responsive and osteoanabolic Wnt signalling pathway) and RANKL (negatively-
216 regulated target gene of Wnt signalling) which have both previously been associated with the
217 mechanical regulation of bone adaptation and healing [8,20-24]. Less abundant Sclerostin staining
218 was visible in the fracture callus compared to the cortical bone of the loaded animal (Fig. 4 f
219 and 5b) with no region-specific differences in staining patterns being seen in the control
220 animal (Fig. 4g and Fig. 5b), suggesting that Wnt-signalling contributes to the loading-
221 mediated osteoanabolic effects on fracture healing seen in this study. At the same time
222 RANKL, which is down-regulated by Wnt-signalling, was more abundantly and stronger

223 expressed in the callus of the loaded animal compared to the control animal (Fig. 4 h+i and
224 Fig. 5b). In line with previous studies, strong RANKL expression was seen in lowly strained
225 callus regions as visualized via micro-FE analysis (Fig. 4a and 5b), indicating ongoing bone
226 remodelling.
227
228 **Discussion**
229 In this study, the effect of individualized cyclic mechanical loading on the remodelling phase
230 of fracture healing was assessed in a novel femur defect loading model in mice using a recently
231 developed *in vivo* micro-CT based monitoring approach. Given the strong mechano-
232 responsiveness of bone cells, several studies have applied mechanical loading (e.g. globally via
233 vibration platforms, or locally via external fixators) to improve fracture healing showing
234 contradictory results. Whereas some studies saw a loading-mediated improvement of fracture
235 healing, others were not successful or even reported an impairment of the fracture healing
236 process [9-11]. One limitation of these studies was the application of the same load to all animals
237 irrespective of individual differences in healing progression, which bears the risk of re-
238 fracturing lowly mineralized bone after initial bridging of the defect. In order to allow for
239 individualized mechanical loading we now developed a precisely controlled *in vivo* loading
240 model based on external fixation of femur defects in mice. By combining state-of-the-art time-
241 lapsed *in vivo* imaging with individualized mechanical loading protocols adapted to animal-
242 specific callus properties, this allows to precisely characterize spatio-temporal effects of
243 mechanical loading on the fracture callus. Given the high mechano-responsiveness of bone
244 cells during normal bone remodelling and as recent studies also indicate a potential to
245 improve fracture healing outcome via modulation of callus remodelling [13-15], we focused this

246 study on the effect of mechanical loading on callus properties during the remodelling phase
247 of fracture healing.

248 Via weekly *in vivo* micro-CT imaging, we saw, that cyclic mechanical loading linearly increased
249 the osseous callus volume during the remodelling phase of fracture healing, so that by the
250 study end, loaded animals had significantly more bone in all callus VOIs (2x for DC, $p<0.0001$;
251 4x for DP, $p<0.0001$; 3x for FP, $p<0.0001$) with a significantly larger fraction of highly
252 mineralized bone compared to controls (+8% for DC, $p=0.0006$; +15% for DP, $p<0.0015$; +10%
253 for FP, $p<0.0001$). This is supported by recent study from Liu et al. [25] describing additional
254 loading-mediated bone formation during the remodelling phase in a uni-cortical tibia defect
255 model in mice. However, they failed to show statistical significance between the loading and
256 the control group in histomorphometry and micro-CT analyses, which they attributed to the
257 high variability within groups. As the study applied the same load to all animals irrespective of
258 healing progression, differences in the induced strains might have caused the high variability
259 within groups. We addressed this by using our recently developed RTFE based loading
260 approach [26], which takes into account the individual strain distribution within the callus for
261 determining individual loading settings at weekly post-operative intervals. In a recent study
262 by Malhotra et al. [27] individualized cyclic mechanical loading (week 0 – week 4, 3x/week) was
263 shown to significantly increase bone volume fraction in a partial vertebral defect model
264 compared to controls. So far, no study using a complete defect model assessed the effect of
265 local cyclic mechanical loading (e.g. via external fixators, tibia/ulna-loading) when exclusively
266 applied during the remodelling phase of the healing process. An earlier tibia defect loading
267 study (defect size: 3 mm) in sheep by Goodship et al. [6] applied cyclic mechanical loading (25
268 µm interfragmentary movement, 30 Hz) throughout the healing period (week 0 - week 10, 5x

269 per week) and reported a significantly larger callus with higher mineralization in loaded
270 animals compared to controls. However, as the loading application was not restricted to
271 specific post-operative time frames, it was not possible to evaluate whether loading during a
272 specific fracture healing period was sufficient for the observed improvement in fracture
273 healing or if cyclic mechanical loading needs to be applied throughout the healing process to
274 achieve such an effect. We now showed, that the remodelling phase is highly responsive to
275 cyclic mechanical loading applied after initial cortical bridging of the defect, with pronounced
276 effects on callus size and mineralization. Via limiting the loading application to the earlier
277 healing period (day 7 – day 19), Gupta et al. [28] aimed at assessing (histomorphometry and
278 radiography on day 42) whether there is a sustained effect of cyclic mechanical loading (2%,
279 10% and 30% strain, 0.5 Hz, 500 cycles) on fracture healing outcome. They found a larger bone
280 fraction in the callus and higher cortical bridging scores in the loaded compared to the control
281 animals, indicating, that loading effects persisted after a 4-week non-loading period. In
282 contrast to these studies, Schwarz et al. [29] did not observe any loading-mediated improvement
283 on fracture healing in a critically-sized femur defect model in rats (defect size: 5mm). However,
284 in this study loading (6 cycles of constant loading at 500 µm IFM and 40s rest phase), was only
285 applied once per week, which indicates a critical role of the type of loading (constant vs. cyclic)
286 and the frequency of loading sessions per week. Whether cyclic mechanical loading in contrast
287 to constant mechanical loading is able to prevent non-union formation in critically-sized
288 defects needs to be assessed in future studies.
289 We were now able to also include dynamic parameters such as bone formation and resorption
290 in the monitoring of loading-mediated effects on fracture healing via registration of
291 longitudinal *in vivo* micro-CT scans (for details see Tourolle et al. 2019 [19]). Compared to

292 histology-based determination of the bone formation rate via *in vivo* application of fluorescent
293 dyes (e.g. calcein, alizarin), our micro-CT-based monitoring approach with registration of
294 consecutive scans also allows for assessment of the bone resorption rate in individual animals,
295 which was shown to be particularly suited for the characterization of the remodelling phase
296 during the fracture healing process [18,30]. The most striking loading-mediated effect in the
297 current study was the prompt and significant reduction in bone resorption rate (week 3-4 vs.
298 week 2-3), which was seen in the central and periosteal VOIs (DC, FP) as early as 1 week after
299 loading (Fig. 3A, 3J). Compared to control animals, in which bone resorption still increased
300 during this early remodelling period (week 3-4), loaded animals showed significantly lower
301 bone resorption rates in all callus VOIs (DC, DP, FP) in this first week of loading, indicating a
302 strong mechano-responsiveness of the fracture callus during this healing period. Most of the
303 previous studies either assessed the loading effects only after a longer loading period of
304 minimum 2 weeks [29,31] or they did not see significant loading-mediated effects on the fracture
305 callus after shorter treatment periods [8,10,28]. So far only one study by Leung et al. [32] was able
306 to detect a loading-mediated improvement of fracture healing (larger callus diameter) after a
307 short loading period of 1 week. We were now able to strengthen these cross-sectional
308 structural callus findings with our longitudinal micro-CT data obtained for single animals. In
309 respect to the underlying mechanisms, we showed for the first time, that not only bone
310 formation but also bone resorption can be significantly modulated via cyclic mechanical
311 loading during fracture healing, indicating a potential for mechanical intervention therapies
312 to improve impaired fracture healing conditions associated with imbalanced bone
313 remodelling. Furthermore, implementation of our two-threshold approach showed cyclic
314 mechanical loading to be also effective in significantly advancing callus mineralization

315 compared to control animals. Via combining our novel loading model with time-lapsed *in vivo*
316 imaging and a two-threshold approach, we were able to characterize the spatio-temporal
317 effects of loading during the remodelling phase of fracture healing. Furthermore, the applied
318 micro-FE-based loading approach also allowed for spatio-temporal visualization of strains
319 induced in the fracture callus (Fig. 4a+b). In order to also visualize the tissue composition of
320 the callus, we performed end point histological stainings of serial sections from one animal of
321 each group. Histology supported our micro-CT findings with complete cortical bridging seen
322 in both groups. However, the loaded animal showed a larger callus with some cartilage
323 fractions suggesting ongoing endochondral ossification processes, whereas in the control
324 animal the callus was largely remodelled with restoration of the medullary cavity indicating
325 proceeding towards the end of healing. Furthermore, differences in the shape of the cell nuclei
326 were seen between the osteocytes in the fracture callus (round shape) of the loaded animal
327 in comparison to the cell nuclei seen in the cortical bone of the same animal (ellipsoidal shape)
328 and the cell morphology seen in the control animals. This is particularly interesting, as previous
329 *in vitro* studies found, that round cells are more sensitive to mechanical loading compared to
330 flat and elongated cells [33-35], suggesting that repeated cyclic mechanical loading might be able
331 to induce round cellular morphology of (early) osteocytes, thereby maintaining the
332 remodelling phase of fracture healing eventually leading to higher mineralization of the newly
333 formed tissue compared to controls. In the *in vivo* setting osteocytes reside in lacunae within
334 the lacunocanalicular network (LCN). A recent study by Casanova et al. [36] longitudinally
335 assessed the development and evolution of the LCN during fracture healing indicating a
336 progressive increase in the complexity of the LCN, which they attributed to factors expressed
337 by osteocytes such as matrix metalloproteinases, Sclerostin and RANKL. To capture potential

338 underlying molecular targets of the spatio-temporal loading effects seen in the current study,
339 we performed immunohistochemistry of Sclerostin (inhibitor of the mechano-responsive and
340 osteoanabolic Wnt signalling pathway) and RANKL (negatively-regulated target gene of Wnt
341 signalling) which have both previously been associated with the mechanical regulation of bone
342 adaptation and healing [8,20-24]. Whereas visual inspection showed less abundant Sclerostin
343 staining in the fracture callus compared to the cortical bone of the loaded animal (Fig. 4f, Fig.
344 5b), no region-specific differences in staining patterns were seen in the control animal (Fig.
345 4g, Fig. 5b). This might indicate that Wnt-signalling contributes to the loading-mediated
346 osteoanabolic effects on fracture healing seen in this study. However, at the same time we
347 saw more and stronger RANKL staining in the callus of the loaded animal compared to the
348 control animal (Fig. 4 h+i). This finding precludes that the loading-mediated increases in RANKL
349 expression seen in this study were solely mediated via Wnt-signalling but rather an interplay
350 with further signalling pathways must have triggered this strong response in RANKL
351 production. Via micro-FE analysis, we saw high RANKL expression in the lowly strained
352 endosteal fracture callus, indicating ongoing bone remodelling. In order to shed light into the
353 complex interplay between a multitude of mechano-responsive molecules and signalling
354 pathway, novel advents in RNAsequencing including spatial transcriptomic approaches might,
355 in future studies, open interesting possibilities to understand the spatio-temporal
356 mechanomics of fracture healing. In non-fractured bone, some of these molecular
357 technologies (e.g. microarrays, [37-40]) have already been successfully applied to study mechano-
358 molecular effects in well-controlled and characterized loading models (e.g. ulna, tibia and tail
359 loading) in rodents. Targets (e.g. Sclerostin, Estrogen signalling) found via these
360 comprehensive studies were then assessed in detail in further studies using either models

361 with local [41-43] or global load application [44]. As the main underlying mechanisms of bone
362 adaptation to loading were identified using local loading models of long bones (ulna, tibia ..),
363 this indicates that comprehensive spatio-temporal mechano-molecular analyses in fracture
364 healing will require tightly regulated models with local application of mechanical loading being
365 more controllable and less prone to variation induced by confounding factors compared to
366 models with global loading application.
367 In summary, using our recently developed femur defect loading model in combination with
368 time-lapsed *in vivo* micro-CT and a two-threshold approach, we showed that the remodelling
369 phase of fracture healing is highly responsive to cyclic mechanical loading with changes in
370 dynamic callus parameters leading to larger callus formation and mineralization. Loading-
371 mediated maintenance of callus remodelling was associated with distinct effects on the Wnt-
372 signalling-associated molecular targets Sclerostin and RANKL in callus sub-regions and the
373 adjacent cortex as assessed via immunohistochemistry. Given these distinct local protein
374 expression patterns induced by external cyclic mechanical loading, our tightly-controlled
375 femur defect loading model with individualized load application could be used in future
376 studies to precisely understand the local spatio-temporal mechano-molecular regulation of
377 the different fracture healing phases. With our RTFE based approach for individualized load
378 application considering differences in defect geometry and healing progression, the femur
379 defect loading model could also be used to study the bone regeneration capacity of
380 biomaterials under load application. With further advents in transcriptomics and registration
381 techniques for different imaging technologies, the tightly controlled femur defect loading
382 model could widen our knowledge on the local spatio-temporal mechano-molecular

383 regulation of fracture healing relevant for application of mechanical intervention therapies to
384 clinical settings for improvement of impaired healing conditions.
385
386 **Methods**
387 **Study design**
388 By combining a novel *in vivo* femur defect loading model with a recently established time-
389 lapsed *in vivo* micro-CT based monitoring approach, the influence of individualized cyclic
390 mechanical loading on callus properties was assessed during the remodelling phase of fracture
391 healing. All mice received a femur defect and post-operative micro-CT scans (vivaCT 40,
392 ScancoMedical, Brüttisellen, Switzerland) were performed. After bridging of the femur defect
393 (week 3), RTFE allowed determination of initial loads (8N-12N), and weekly load-scaling and
394 matching of strain distribution in the callus for the 4 week loading period. The loading group
395 (n=10) received individualized cyclic mechanical loading (8-16N, 10 Hz, 5 min, 3x/week)
396 whereas controls (n=10) received 0N for 5 min at the same post-operative time-points. By
397 registration of consecutive scans, structural and dynamic callus parameters were followed in
398 three callus sub-volumes (defect centre: DC, defect periphery: DP, cortical fragment
399 periphery: FP) and the adjacent cortical fragments (FC) over time (Figure 3, for details on
400 methods see Tourolle et al. 2020[19]; for detailed study design see Supplementary Table S1).
401
402 **Animals**
403 All animal procedures were approved by the Commission on Animal Experimentation (license
404 number: 181/2015; Kantonales Veterinäramt Zürich, Zurich, Switzerland). We confirm that all
405 methods were carried out in accordance with relevant guidelines and regulations (Swiss

406 Animal Welfare Act and Ordinance (TSchG, TSchV)) and reported considering ARRIVE
407 guidelines. To study adult fracture healing female 12 week-old C57BL/6J mice were purchased
408 from Janvier (Saint Berthevin Cedex, France) and housed in the animal facility of the ETH
409 Phenomics Center (EPIC; 12h:12h light-dark cycle, maintenance feed (3437, KLIBA NAFAG,
410 Kaiseraugst, Switzerland), 5 animals/cage) for 8 weeks. At an age of 20 weeks, all animals
411 received a femur defect by performing an osteotomy with a 0.66mm Gigli wire saw as
412 previously described (group 1: control group, n=10; group 2: loading group, n=10; housing
413 after surgery: 2-3 animals/cage; for details on study design see Supplementary Table 1). All
414 defect surgeries were performed by the same veterinarian. Perioperative analgesia (25 mg/L,
415 Tramal®, Gruenenthal GmbH, Aachen, Germany) was provided via the drinking water two days
416 before surgery until the third post-operative day. For surgery and micro-CT scans, animals
417 were anaesthetized with isoflurane (induction/maintenance: 5%/1-2% isoflurane/oxygen).
418 Perioperative handling, and monitoring, micro-CT imaging and loading application was
419 performed by the surgeon.
420
421 **Loading fixator assembly and group assignment**
422 The four parts of the loading fixators (n=20) were assembled as depicted in Fig. 1. To allow
423 optimal identification throughout the experiments, one side part was engraved with a fixator-
424 specific number (Fig 1a, 1b). The stiffness of each fixator was measured using a Zwick testing
425 machine and the fixators were assigned to the two groups, to allow similar distributions of
426 fixator stiffness in the loading and control group (Supplementary Fig. 3).
427
428 **Femur osteotomy**

429 In all animals an external fixator (Mouse ExFix, RISystem, Davos, Switzerland; mean stiffness:
430 17N/mm; Suppl. Fig. 1) was positioned at the craniolateral aspect of the right femur and
431 attached using four mounting pins. First, the most proximal pin was inserted approximately
432 2mm proximal to the trochanter, followed by placement of the most distal and the inner pins.
433 Subsequently, a femur defect was created using a Gigli wire (diameter: 0.66mm).
434

435 **Time-lapsed *in vivo* micro-CT**

436 Immediate post-surgery correct positioning of the fixator and the defect was visualized using
437 a vivaCT 40 (Scanco Medical AG, Brüttisellen, Switzerland) (isotropic nominal resolution: 10.5
438 µm; 2 stacks of 211 slices; 55 kVp, 145 µA, 350 ms integration time, 500 projections per 180°,
439 21 mm field of view (FOV), scan duration ca. 15 min). Subsequently, the fracture callus and
440 the adjacent bone between the inner pins of the fixator were scanned weekly using the same
441 settings. Scans were registered consecutively using a branching scheme (registration of whole
442 scan for bridged defects; separate registration of the two fragments for unbridged defects)[5].
443 Subsequently, morphometric indices (bone volume - BV, bone volume/total volume – BV/TV,
444 bone formation rate – BFR, bone resorption rate - BRR) were computed (threshold: 395mg
445 HA/cm^3; for details on methods see Tourolle et al., 2020 [19]). To assess mineralization
446 progression, a second threshold (645mg HA/cm^3) was applied and the ratio between highly
447 and lowly mineralized tissue (BV_{645}/BV_{395}) was calculated. The two selected thresholds are
448 included in our recently developed multidensity threshold approach [19]. According to the
449 standard clinical evaluation of X-rays, the number of bridged cortices per callus was evaluated
450 in two perpendicular planes (UCT Evaluation V6.5-1, Scanco Medical AG, Brüttisellen,

451 Switzerland). A ‘‘healed fracture’’ was considered as having a minimum of at least three
452 bridged cortices per callus.
453 For evaluation, four volumes of interest (VOIs) were defined, which were created
454 automatically from the post-operative measurement (Fig. 3): defect centre (DC), defect
455 periphery (DP), cortical fragment centre (FC), and fragment periphery (FP). Data were
456 normalised to the central VOIs: DC/DC, DP/DC, FC/FC, FP/FC.
457

458 **Individualized cyclic mechanical loading**

459 From week 4 to week 7, individualized cyclic loading (8-16N, 10Hz, 3000cycles; 3x/week;
460 controls - 0N) was applied via the external loading fixator (Fig 1b) based on computed strain
461 distribution in the callus using animal-specific RTFE analysis (for detailed description of
462 methods see [26]). Briefly, after weekly micro-CT measurements of each animal, the images
463 were pre-processed using threshold-binning to create a high-resolution multi-density FE
464 mesh, which was then solved on a supercomputer within the same anaesthetic session for
465 each mouse. 2D and 3D visualizations of the callus were generated and a strain histogram was
466 plotted. This information allowed load scaling based on the strains induced in the callus in
467 individualized animals. Specifically, the distribution was scaled to achieve a median effective
468 microstrain of 700. To assess regions that posed a failure risk the 99th percentile strains of
469 each simulation was visualised in both image based and histogram forms. If more than 50
470 voxels exceeded 1% then the optimised load was reduced by 1 N.
471

472 **Mechanical testing**

473 3 point bending tests were performed on a Zwick compression tester (ZwickRoell GmbH & Co,
474 Ulm, Germany). Tests were conducted on a setup of 8 mm support span and up to 3 N. Tests
475 were performed quasi-statically with a cross-head speed of 0.4 mm/min. Stiffness was then
476 calculated from the linear region of the resultant force-displacement curve. Each sample was
477 tested three times and the mean stiffness was taken.
478
479
480 **Histology**
481 Histological stainings were performed in one animal per group. On day 49, femora were
482 excised, the femoral head was removed and the samples were placed in 4% neutrally buffered
483 formalin for 24 hours and subsequently decalcified in 12.5% EDTA for 10-14 days. The samples
484 were embedded in paraffin and the complete fracture callus was cut in 10 µm longitudinal
485 serial sections. Every 10th section was stained with Safranin-O: Weigert's iron haematoxylin
486 solution (HT1079, Sigma-Aldrich, St. Louis, MO) - 4min, 1:10 HCl-acidified 70% ethanol - 10s,
487 tap water - 5min, 0.02% Fast Green (F7258, Sigma-Aldrich, St. Louis, MO) - 3min, 1% acetic
488 acid - 10s, 0.1% Safranin-O (84120, Fluka, St. Louis, MO) - 5min. Images were taken with Slide
489 Scanner Pannoramic 250 (3D Histech, Budapest, Hungary) at 20x magnification. Sections in
490 between were stained for Sclerostin and RANKL.
491 For immunohistochemical staining of Sclerostin, nonspecific sites were blocked (1% BSA/PBS
492 + 1% rabbit serum) for 60 min at room temperature. Subsequently, the sections were
493 incubated with the primary antibody against Sclerostin (AF1589, R&D Systems, Minneapolis,
494 MN; 1:150 in 1%BSA/PBS + 0.2% rabbit serum) overnight at 4°C. To detect the primary
495 antibody, a secondary biotinylated rabbit anti-goat-IgG antibody (BAF017, R&D Systems,

496 Minneapolis, MN) was added for 1 h at room temperature. For signal amplification, the slides
497 were incubated with avidin-biotin complex (PK-6100 Vector Laboratories, Burlingame, CA) for
498 30 min. Diaminobenzidine (Metal Enhanced DAB Substrate Kit, 34065 ThermoFisher Scientific,
499 Waltham, MA) was used as detection substrate. Counterstaining was performed with
500 FastGreen (F7258, Sigma-Aldrich, St. Louis, MO).
501 For immunohistochemical staining of RANKL, slides were placed into TBS-Tween buffer and
502 inserted into the Dako-Autostainer (Dako, Ft. Collins, USA) using the following staining
503 protocol: incubation with primary antibody against RANKL (1:100; ab 9957, Abcam,
504 Cambridge, UK) at 4°C overnight, rinsing with TBS-Tween, peroxidase blocking for 10min at
505 room temperature, rinsing with TBS-Tween, Envision+System HPR Rabbit (Dako K4003) for 60
506 min at room temperature, rinsing with TBS-Tween and incubation with DAB (Dako K3468) for
507 10 min at room temperature. The slides were rinsed in A. dest and counterstained with
508 FastGreen for 2sec.
509 For both immunohistochemical stainings, species-specific IgG was used as isotype control.
510 Images were taken with Slide Scanner Pannoramic 250 (3D Histech, Budapest, Hungary) at 40x
511 magnification.
512
513 **Statistics**
514 Data were tested for normal distribution (Shapiro-Wilk-Test) and homogeneity of variance
515 (Levene-Test). Depending on the test outcome, group comparisons (loading vs. control group)
516 of data derived at single time points (VOI size) were performed by two-tailed Student's t-test
517 or Mann-Whitney U-test (IBM SPSS Statistics Version 23). For statistical evaluation of repeated

518 measurements two-way ANOVA with Geisser-Greenhouse correction and Bonferroni
519 correction (GraphPad Prism 8) were performed. The level of significance was set at $p < 0.05$.
520

521 **Acknowledgements**

522 We thank Marco Hitz and Peter Schwilch for technical assistance. We thank Dr. Angad
523 Malhotra and Jianhua Zhang for surgery assistance. We thank Christopher M. O'Neill for the
524 micro-CT and micro-FE images depicted in Figure 4. The authors gratefully acknowledge
525 support from the EU (ERC Advanced MechAGE ERC-2016-ADG-741883). E. Wehrle received
526 funding from the ETH Postdoctoral Fellowship Program (MSCA-COFUND, FEL-25_15-1).
527

528 **Author Contributions Statement**

529 The study was designed by E.W., G.A.K., and R.M.. The experiments were performed by E.W.
530 and G.R.P. Data analyses were performed by E.W., G.R.P. and D.C.B.. The manuscript was
531 written by E.W. and reviewed and approved by all authors.
532

533 **Data availability**

534 All necessary data generated or analysed during the present study are included in this
535 published article and its Supplementary Information files (preprint available on BioRxiv
536 (BIORXIV/2020.09.15.297861). Additional data that support the findings of this study are
537 available from the corresponding author upon reasonable request.
538

539 **Competing Interests**

540 The authors declare no competing interests.

References

1 Einhorn, T. A. & Gerstenfeld, L. C. Fracture healing: mechanisms and interventions. *Nat Rev Rheumatol* **11**, 45-54, doi:10.1038/nrrheum.2014.164 (2015).

2 Gomez-Barrena, E. *et al.* Bone fracture healing: Cell therapy in delayed unions and nonunions. *Bone* **70**, 93-101, doi:10.1016/j.bone.2014.07.033 (2015).

3 Bottlang, M. *et al.* Effects of Construct Stiffness on Healing of Fractures Stabilized with Locking Plates. *J Bone Joint Surg Am* **92a**, 12-22, doi:10.2106/Jbjs.J.00780 (2010).

4 Steiner, M., Claes, L., Ignatius, A., Simon, U. & Wehner, T. Numerical Simulation of Callus Healing for Optimization of Fracture Fixation Stiffness. *Plos One* **9**, doi:ARTN e10137010.1371/journal.pone.0101370 (2014).

5 Claes, L. E. & Heigele, C. A. Magnitudes of local stress and strain along bony surfaces predict the course and type of fracture healing. *J Biomech* **32**, 255-266, doi:Doi 10.1016/S0021-9290(98)00153-5 (1999).

6 Goodship, A. E., Lawes, T. J. & Rubin, C. T. Low-Magnitude High-Frequency Mechanical Signals Accelerate and Augment Endochondral Bone Repair: Preliminary Evidence of Efficacy. *J Orthop Res* **27**, 922-930, doi:10.1002/jor.20824 (2009).

7 Shi, H. F., Cheung, W. H., Qin, L., Leung, A. H. C. & Leung, K. S. Low-magnitude high-frequency vibration treatment augments fracture healing in ovariectomy-induced osteoporotic bone. *Bone* **46**, 1299-1305, doi:10.1016/j.bone.2009.11.028 (2010).

8 Wehrle, E. *et al.* The impact of low-magnitude high-frequency vibration on fracture healing is profoundly influenced by the oestrogen status in mice. *Dis Model Mech* **8**, 93-104, doi:10.1242/dmm.018622 (2015).

9 Stuermer, E. K. *et al.* Musculoskeletal Response to Whole-Body Vibration During Fracture Healing in Intact and Ovariectomized Rats. *Calcified Tissue Int* **87**, 168-180, doi:10.1007/s00223-010-9381-0 (2010).

10 Wehrle, E. *et al.* Distinct Frequency Dependent Effects of Whole-Body Vibration on Non-Fractured Bone and Fracture Healing in Mice. *J Orthop Res* **32**, 1006-1013, doi:10.1002/jor.22629 (2014).

11 Wolf, S. *et al.* Effects of high-frequency, low-magnitude mechanical stimulus on bone healing. *Clin Orthop Relat R*, 192-198 (2001).

12 Wang, J., Leung, K. S., Chow, S. K. H. & Cheung, W. H. The Effect of Whole Body Vibration on Fracture Healing - a Systematic Review. *Eur Cells Mater* **34**, 108-127, doi:10.22203/eCM.v034a08 (2017).

13 Bao, Q. W. *et al.* An appropriate Wnt/beta-catenin expression level during the remodeling phase is required for improved bone fracture healing in mice. *Sci Rep-Uk* **7**, doi:ARTN 269510.1038/s41598-017-02705-0 (2017).

14 Hegde, V., Jo, J. E., Andreopoulou, P. & Lane, J. M. Effect of osteoporosis medications on fracture healing. *Osteoporosis Int* **27**, 861-871, doi:10.1007/s00198-015-3331-7 (2016).

15 Schindeler, A., McDonald, M. M., Bokko, P. & Little, D. G. Bone remodeling during fracture repair: The cellular picture. *Semin Cell Dev Biol* **19**, 459-466, doi:10.1016/j.semcdb.2008.07.004 (2008).

16 Paul, G. R., Wehrle, E., Tourolle, D. C., Kuhn, G. A. & Muller, R. Real-time finite element analysis allows homogenization of tissue scale strains and reduces variance in a mouse defect healing model. *Sci Rep* **11**, 13511, doi:10.1038/s41598-021-92961-y (2021).

17 Wehrle, E. *et al.* Spatio-temporal characterization of fracture healing patterns and assessment of biomaterials by time-lapsed in vivo micro-computed tomography. *Sci Rep* **11**, 8660, doi:10.1038/s41598-021-87788-6 (2021).

18 Wehrle, E. *et al.* Evaluation of longitudinal time-lapsed in vivo micro-CT for monitoring fracture healing in mouse femur defect models. *Sci Rep-Uk* **9**, doi:ARTN 1744510.1038/s41598-019-53822-x (2019).

19 Tourolle né Betts D.C., W. E., Pau G.R., Kuhn G.A., Christen P., Hofmann S, Müller R. The association between mineralised tissue formation and the mechanical local in vivo environment: Time-lapsed quantification of a mouse defect healing model. *Sci Rep-Uk* **10**, doi:https://doi.org/10.1038/s41598-020-57461-5 (2020).

20 Li, C. *et al.* Sclerostin Antibody Treatment Enhances Fracture Healing and Increases Bone Mass and Strength in Non-Fractured Bones in an Adult Rat Closed Femoral Fracture Model. *Osteoporosis Int* **22**, 11-12 (2011).

21 Mcdonald, M. M. *et al.* Bone volume is not altered with unloading in the homozygous sclerostin knockout mouse. *Bone* **50**, S94-S94, doi:10.1016/j.bone.2012.02.282 (2012).

22 Ominsky, M. S. *et al.* Inhibition of Sclerostin by Monoclonal Antibody Enhances Bone Healing and Improves Bone Density and Strength of Nonfractured Bones. *Journal of Bone and Mineral Research* **26**, 1012-1021, doi:10.1002/jbmr.307 (2011).

23 Robling, A. G. *et al.* Mechanical stimulation of bone in vivo reduces osteocyte expression of Sost/sclerostin. *J Biol Chem* **283**, 5866-5875, doi:10.1074/jbc.M705092200 (2008).

24 Suen, P. K. *et al.* Sclerostin Monoclonal Antibody Enhanced Bone Fracture Healing in an Open Osteotomy Model in Rats. *J Orthop Res* **32**, 997-1005, doi:10.1002/jor.22636 (2014).

25 Liu, C. *et al.* Effects of mechanical loading on cortical defect repair using a novel mechanobiological model of bone healing. *Bone* **108**, 145-155, doi:10.1016/j.bone.2017.12.027 (2018).

26 Paul, G. R., Wehrle, E., Tourolle né Betts, D. C., Kuhn, G. & Müller, R. Reducing variance in a mouse defect healing model: Real-time Finite Element Analysis allows homogenization of tissue scale strains *bioRxiv*, doi:10.1101/2020.09.02.274878 (2020).

27 Malhotra, A., Walle, M., Paul, G. R., Kuhn, G. A. & Muller, R. Application of subject-specific adaptive mechanical loading for bone healing in a mouse tail vertebral defect. *Sci Rep* **11**, 1861, doi:10.1038/s41598-021-81132-8 (2021).

28 Gupta, R. R. *et al.* Axial strain enhances osteotomy repair with a concomitant increase in connexin43 expression. *Bone Res* **3**, doi:ARTN 1500710.1038/boneres.2015.7 (2015).

29 Schwarz, C. *et al.* Mechanical Load Modulates the Stimulatory Effect of BMP2 in a Rat Nonunion Model. *Tissue Eng Pt A* **19**, 247-254, doi:10.1089/ten.tea.2012.0265 (2013).

30 Wehrle, E. *et al.* In vivo micro-CT based approach for discrimination of physiological and impaired healing patterns in mouse femur defect models. . *European Cell and Materials* **31**, 168 (2016).

31 Tufekci, P. *et al.* Early mechanical stimulation only permits timely bone healing in sheep. *J Orthop Res* **36**, 1790-1796, doi:10.1002/jor.23812 (2018).

32 Leung, K. S. *et al.* Low-Magnitude High-Frequency Vibration Accelerates Callus Formation, Mineralization, and Fracture Healing in Rats. *J Orthop Res* **27**, 458-465, doi:10.1002/jor.20753 (2009).

33 van Oers, R. F. M., Wang, H. & Bacabac, R. G. Osteocyte Shape and Mechanical Loading. *Curr Osteoporos Rep* **13**, 61-66, doi:10.1007/s11914-015-0256-1 (2015).

34 Vatsa, A. *et al.* Osteocyte morphology in fibula and calvaria - Is there a role for mechanosensing? *Bone* **43**, 452-458, doi:10.1016/j.bone.2008.01.030 (2008).

35 Wu, V. *et al.* Osteocyte morphology and orientation in relation to strain in the jaw bone. *Int J Oral Sci* **10**, doi:Unsp 210.1038/S41368-017-0007-5 (2018).

36 Casanova, M. *et al.* Characterization of the Developing Lacunocanalicular Network During Fracture Repair. *JBMR Plus*, doi: https://doi.org/10.1002/jbm4.10525 (2021).

37 McKenzie, J. A., Bixby, E. C. & Silva, M. J. Differential Gene Expression from Microarray Analysis Distinguishes Woven and Lamellar Bone Formation in the Rat Ulna following Mechanical Loading. *Plos One* **6**, doi:ARTN e2932810.1371/journal.pone.0029328 (2011).

38 Wasserman, E. *et al.* Differential load-regulated global gene expression in mouse trabecular osteocytes. *Bone* **53**, 14-23, doi:10.1016/j.bone.2012.11.017 (2013).

39 Zaman, G. *et al.* Loading-related regulation of gene expression in bone in the contexts of estrogen deficiency, lack of estrogen receptor alpha and disuse. *Bone* **46**, 628-642, doi:10.1016/j.bone.2009.10.021 (2010).

40 Trüssel, A. J. Spatial mapping and high throughput microfluidic gene expression analysis of osteocytes in mechanically controlled bone remodeling. *Doctoral Thesis ETH Zurich*, doi:https://doi.org/10.3929/ethz-a-010465264 (2015).

41 Lara-Castillo, N. *et al.* In vivo mechanical loading rapidly activates beta-catenin signaling in osteocytes through a prostaglandin mediated mechanism. *Bone* **76**, 58-66, doi:10.1016/j.bone.2015.03.019 (2015).

42 Melville, K. M. *et al.* Effects of Deletion of ER in Osteoblast-Lineage Cells on Bone Mass and Adaptation to Mechanical Loading Differ in Female and Male Mice. *Journal of Bone and Mineral Research* **30**, 1468-1480, doi:10.1002/jbmr.2488 (2015).

43 Robling, A. G. *et al.* Sost, independent of the non-coding enhancer ECR5, is required for bone mechanoadaptation. *Bone* **92**, 180-188, doi:10.1016/j.bone.2016.09.001 (2016).

44 Moura, M. L. A. *et al.* Estrogen therapy associated with mechanical vibration improves bone microarchitecture and density in osteopenic female mice. *J Anat* **233**, 715-723, doi:10.1111/joa.12893 (2018).

45 Paul, G. R., Schwilch, P., Wehrle, E., Kuhn, G. A. & Müller, R. Development of a micro-CT mouse holder for a femur defect mouse model. *bioRxiv*, doi:doi: https://doi.org/10.1101/2020.09.10.289553 (2020).

Figure Legends

Figure 1. Loading system for femur defects in mice. a. Loading fixator (RISystem, Davos, Switzerland) consisting of four PEEK parts connected via two transverse Titanium pins. b. Insertion of loading fixator into loading device with clamping of loading adapter (1) and removal of transverse pin (2). c. Loading device consisting of mouse holder with anaesthesia inlet (1), heated ground plate (2), clamp for fixator (3) and actuation system with loading chuck (4), load cell electronics box (5), electro-magnetic actuator (6), actuator control electronic box (7). The mouse holder can be used for the loading device and the CT scanner without the need to change the position of the mouse. For detailed description and drawings see Paul et al. [45].

674 **Figure 2**. Longitudinal imaging of the defect region via micro-CT. Representative images (full
675 image and cut; threshold: 645 mg HA/cm^3) of the defect region from animals of the loading
676 group (week 0-7) and the control group (week 0-7). Visualization of bone formation (orange)
677 and resorption (blue) via registration of micro-CT scans from weeks 1-6 to weeks 0-5.
678
679 **Figure 3**. Micro-CT based evaluation of bone parameters in the defect region during the
680 healing period. Four volumes of interest (VOIs) were assessed in the loading group (red) and
681 the control group (blue) from week 0 – week 7 (pre-loading healing period highlighted in
682 lighter colour; loading period highlighted in darker colour): defect center (DC; a-c), defect
683 periphery (DP; d-f), cortical fragment center (FC; g-i), cortical fragment periphery (FP; j-l). a, d,
684 g, j: Bone formation rate (solid line) and bone resorption rate (dashed line) given in percent
685 per day. b, e, h, k: Bone volume (BV) normalized to TV (DC for DC and DP, FC for FC+FP). c, f, i,
686 l: Degree of bone mineralization given as ratio of bone volume with a density ≥645 mg HA/cm^3
687 to the total osseous volume (threshold ≥395 mg HA/cm^3). n=10 per group; * indicates $p < 0.05$
688 determined by two-way ANOVA with Geisser-Greenhouse correction and Bonferroni
689 correction.
690
691 **Figure 4.** Micro-CT and histological analyses of consecutive callus sections. a, b: Micro-CT
692 images of fracture callus sections corresponding to sections stained with Safranin-O for one
693 animal from the loading (a) and the control group (b): CT image (threshold: 395 mg HA/cm^3),
694 visualization of regions of bone formation and resorption via registration of CT image from
695 weeks 6 and 7, visualization of strains on CT section via micro-FE analysis for week 7 and week
696 6. c-j. Consecutive longitudinal sections of fractured femora 7 weeks after defect surgery of

one animal from the loading group and the control group stained for Safranin-O (c-f), Sclerostin (g, h), RANKL (i, j). Scale bar = 100 µm (c, d), scale bar = 500 µm (e-j).

Figure 5. Visualization of local cellular distribution patterns and protein expression in the fracture callus and adjacent cortex. a. Longitudinal Safranin-O stained sections of fractured femora 7 weeks after defect surgery of one animal from the loading group and one animal from the control group. Boxes indicate regions depicted in b (1: callus; 2: cortex); Scale bar = 100 µm. b. Magnification of callus region (left) and cortical region (right) stained for Safranin-O, Sclerostin and RANKL; Scale bar = 50 µm.

Tables

Table 1. Fracture healing outcome assessed by cortical bridging (healed fracture ≥ 3 bridged cortices, threshold 395 mg HA/cm^3).

		week							
	Group (n=10)	0	1	2	3	4	5	6	7
Healed fractures per group	Control/Loading	0/0	0/0	5/6	9/10	10/10	10/10	10/10	10/10

Figure 1

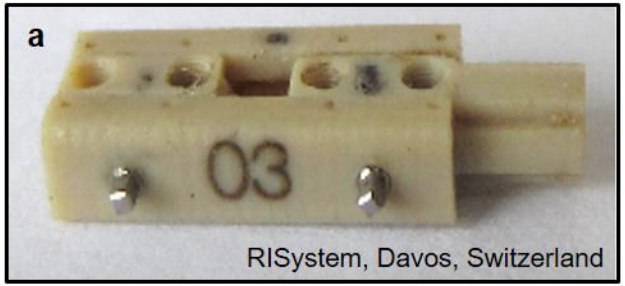
a
03
RISystem, Davos, Switzerland

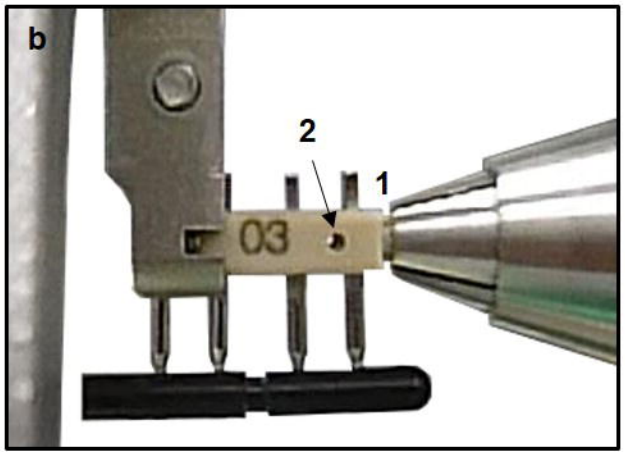
b
2
1
03

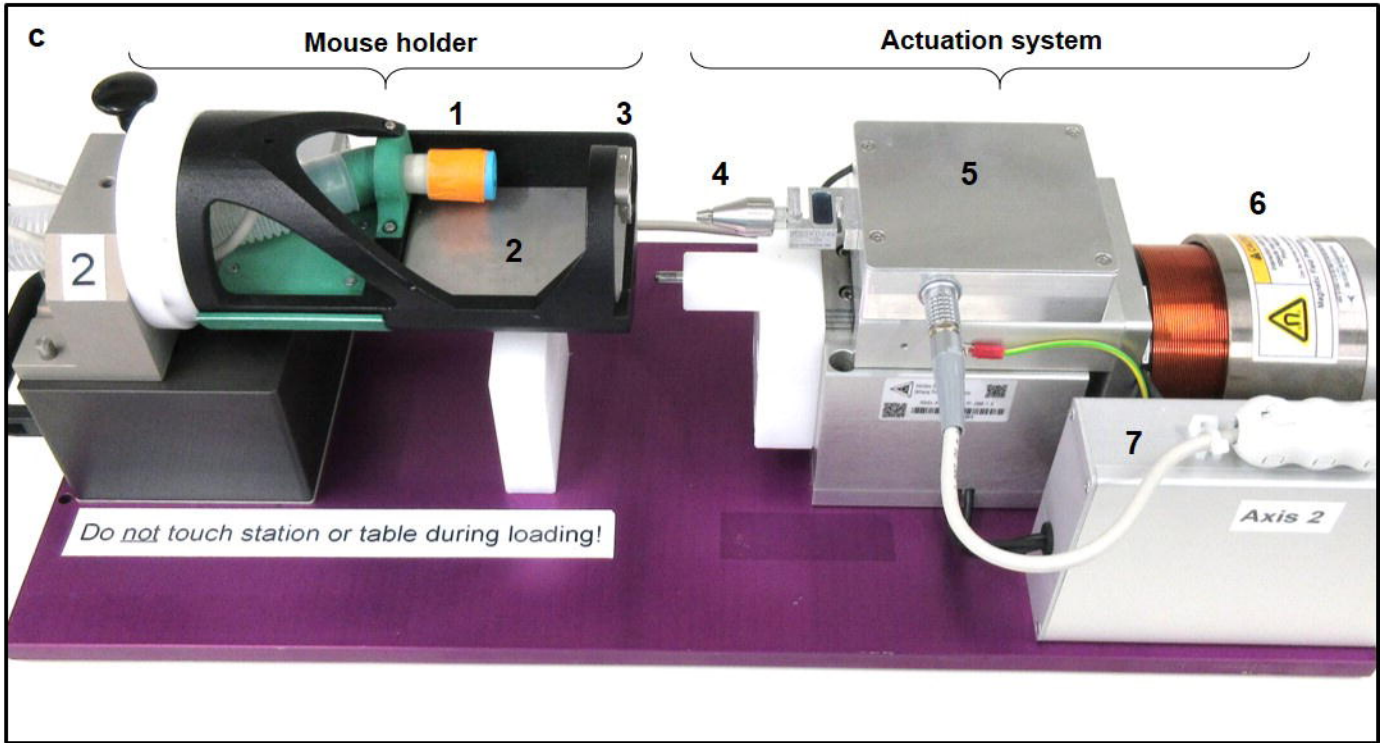
c
Mouse holder
Actuation system
1
3
4
5
6
2
2
7
Do not touch station or table during loading!
Axis 2

Figure 2

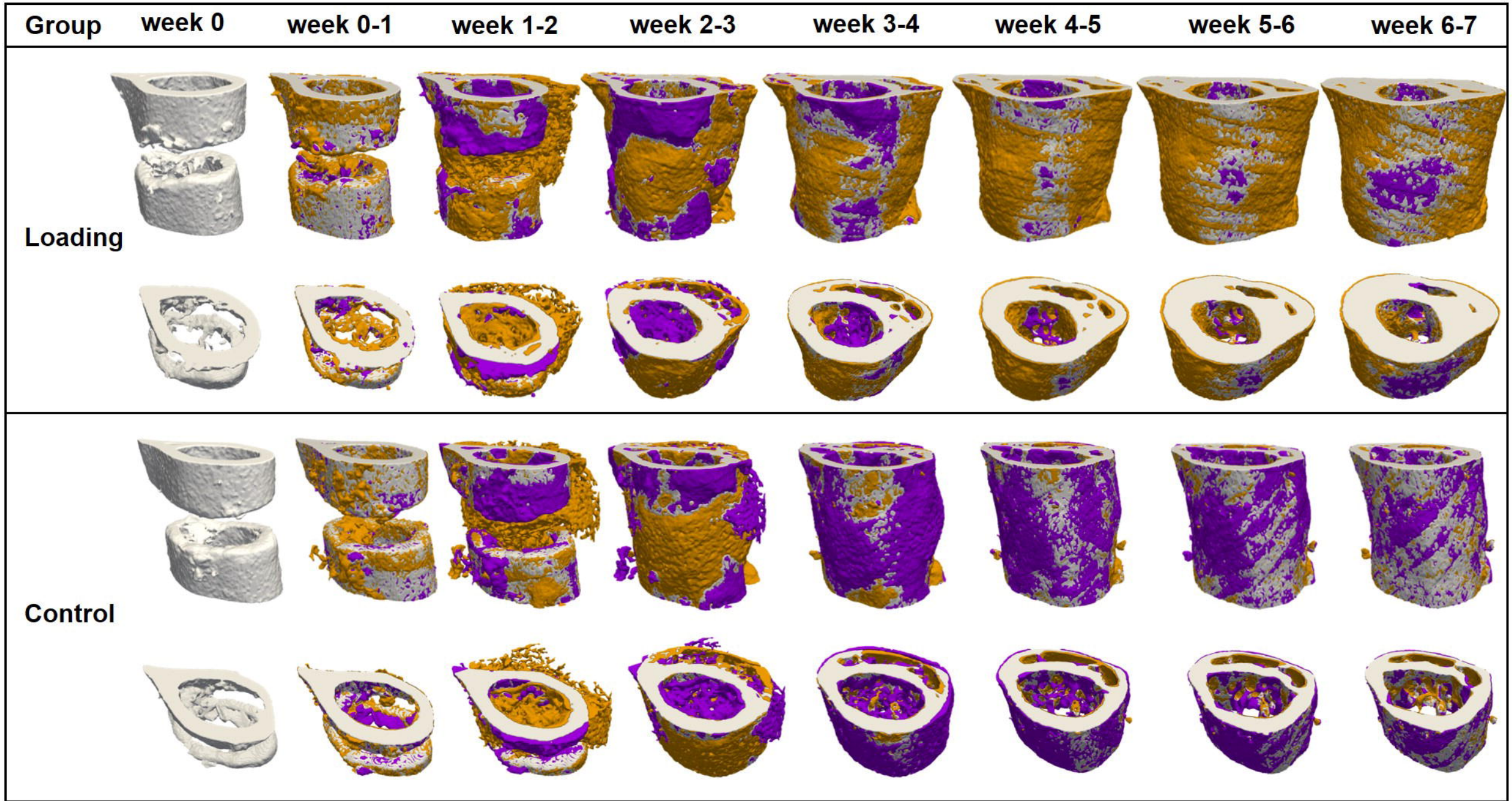
Group
week 0
week 0-1
week 1-2
week 2-3
week 3-4
week 4-5
week 5-6
week 6-7
Loading
Control

Figure 3

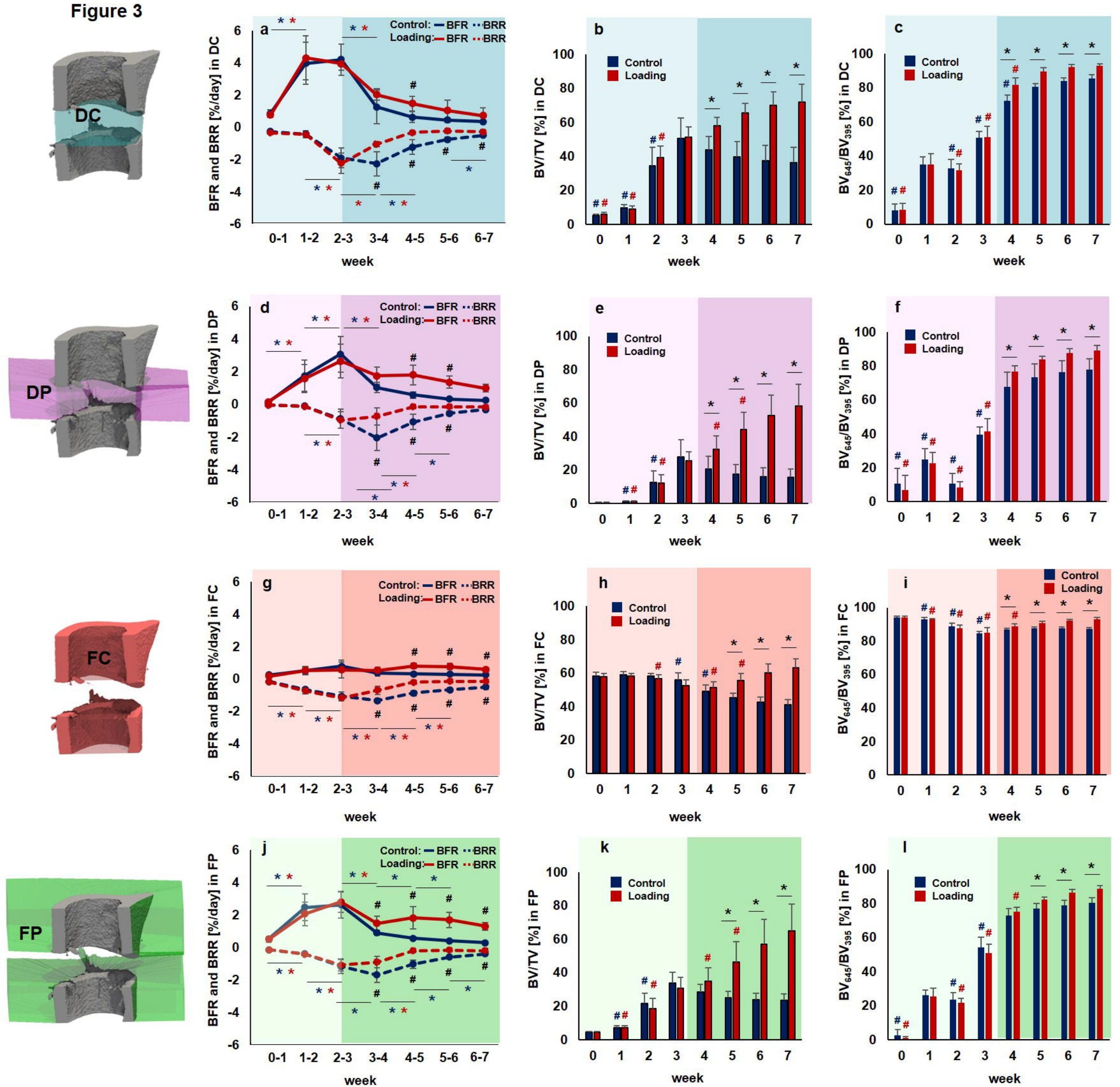
DC
DP
FC
FP
a
b
c
d
e
f
g
h
i
j
k
l
Control: BFR BRR
Loading: BFR BRR
Control
Loading
BFR and BRR [%/day] in DC
BV/TV [%] in DC
BV645/BV395 [%] in DC
BFR and BRR [%/day] in DP
BV/TV [%] in DP
BV645/BV395 [%] in DP
BFR and BRR [%/day] in FC
BV/TV [%] in FC
BV645/BV395 [%] in FC
BFR and BRR [%/day] in FP
BV/TV [%] in FP
BV645/BV395 [%] in FP
0-1 1-2 2-3 3-4 4-5 5-6 6-7
week

Figure 4

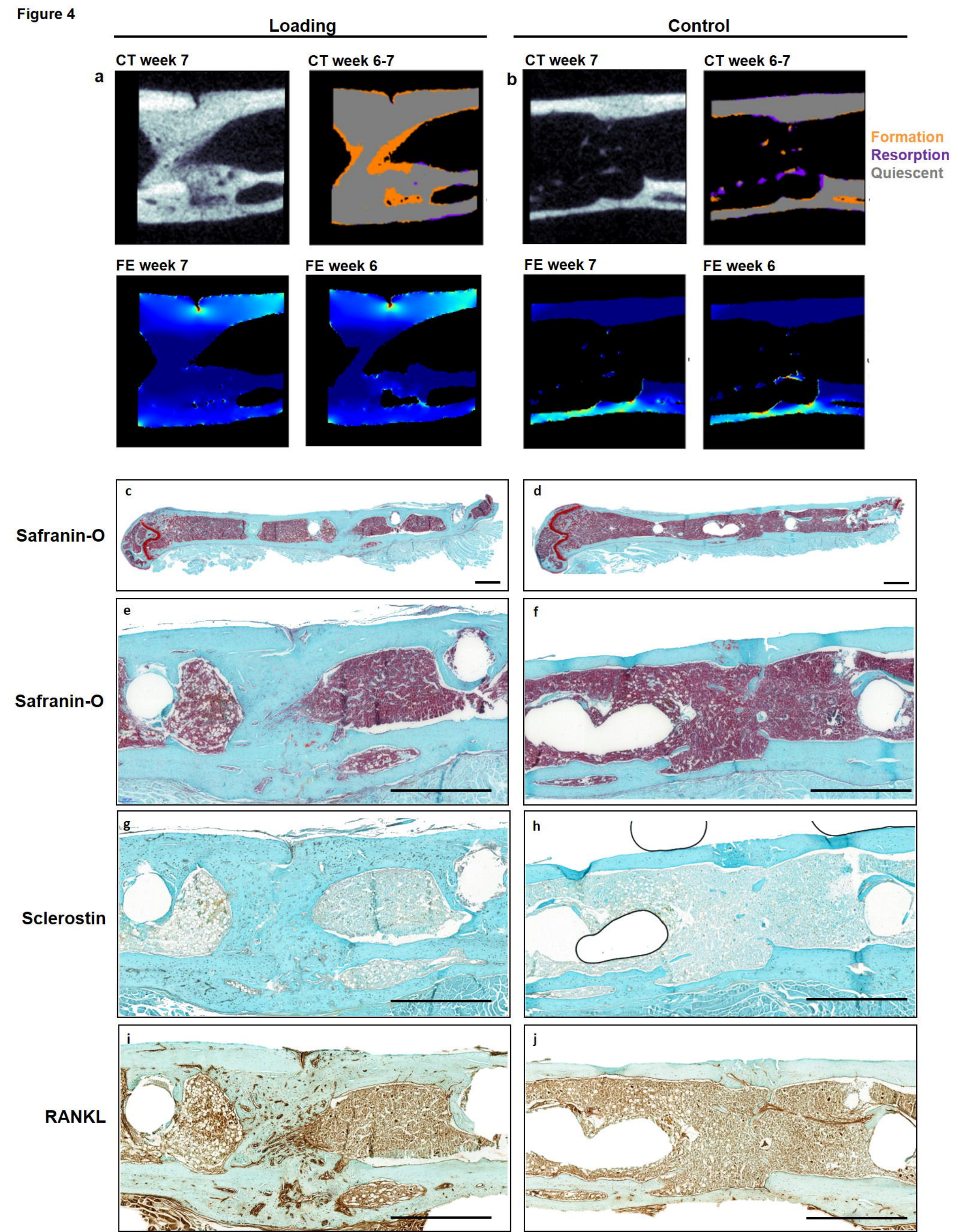
Loading
Control
a
CT week 7
CT week 6-7
FE week 7
FE week 6
b
CT week 7
CT week 6-7
FE week 7
FE week 6
Formation
Resorption
Quiescent
Safranin-O
c
d
Safranin-O
e
f
Sclerostin
g
h
RANKL
i
j

Figure 5

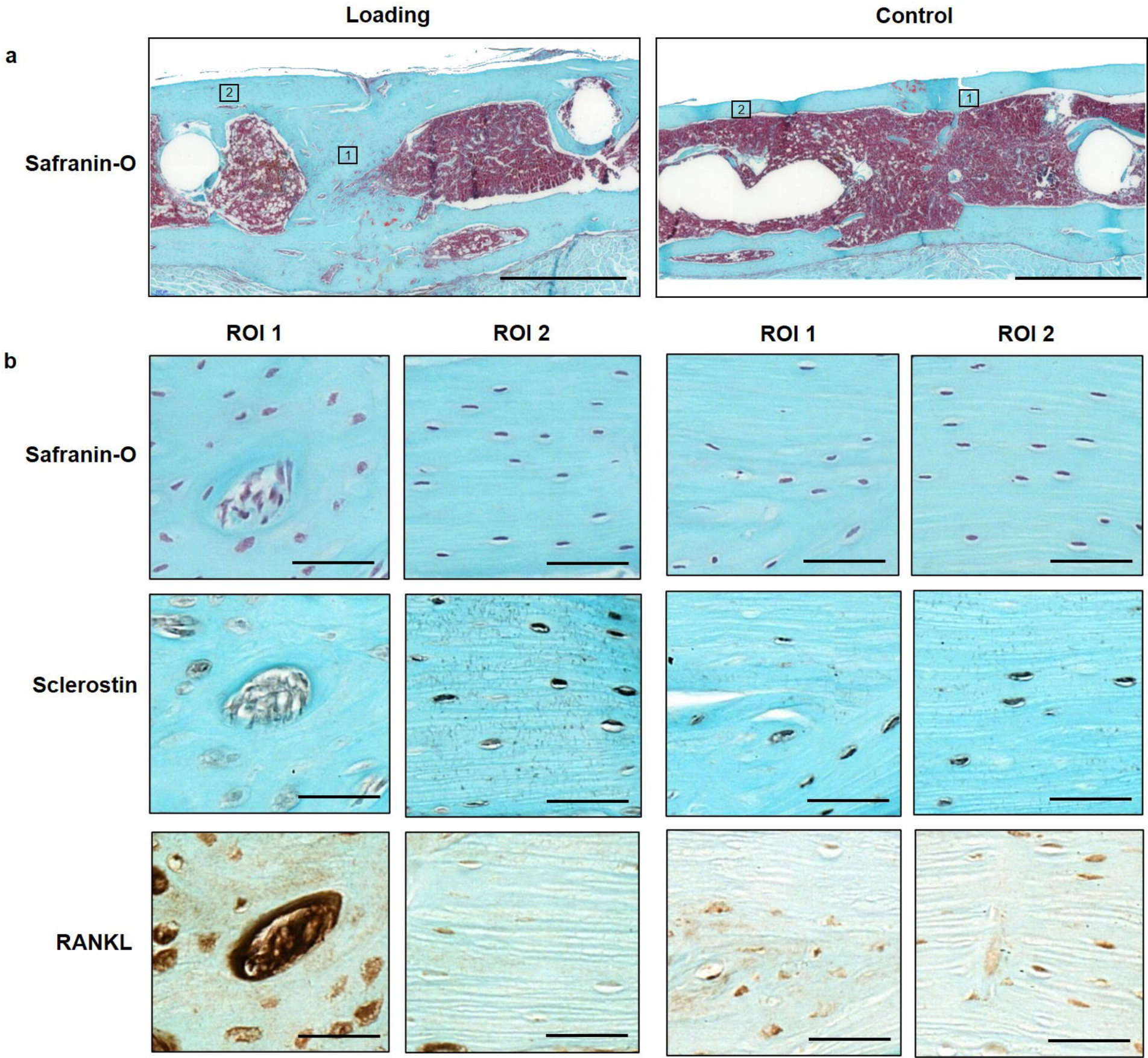
Loading
Control
a
Safranin-O
2
1
2
1
ROI 1
ROI 2
ROI 1
ROI 2
b
Safranin-O
Sclerostin
RANKL